Inorganic Chemistry

pubs.acs.org/IC

Article

Surface Transformations of Lead Oxides and Carbonates Using First-Principles and Thermodynamics Calculations

Ryan T. Grimes, Joshua A. Leginze, Robert Zochowski, and Joseph W. Bennett*

Cite This: *Inorg. Chem.* 2021, 60, 1228−1240

Read Online

ACCESS | Metrics & More | Article Recommendations | SI Supporting Information

ABSTRACT: Lead (Pb)-containing solids find widespread commercial use in batteries, piezoelectrics, and as starting materials for synthesis. Here, we combine density functional theory (DFT) and thermodynamics in a DFT + solvent ion model to compare the surface reactivity of Pb oxides and carbonates, specifically litharge, massicot, and cerussite, in contact with water. The information provided by this model is used to delineate structure−property relationships for surfaces that are able to release Pb as Pb^{2+}. We find that Pb^{2+} release is dependent on pH and chemical bonding environment and go on to correlate changes in the surface bonding to key features of the electronic structure through a projected density of states analysis. Collectively, our analyses link the atomistic structure to i) specific electronic states and ii) the thermodynamics of surface transformations, and the results presented here can be used to guide synthetic efforts of Pb^{2+}-containing materials in aqueous media or be used to better understand the initial steps in solid decomposition.

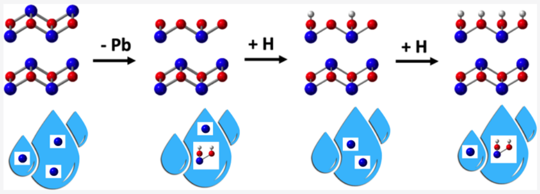

■ INTRODUCTION

The Pb^{2+} cation is a stereochemically active and polarizable soft acid.[1−3] This allows Pb^{2+}-based materials to form from a wide variety of ligand building blocks in which the lone electron pair helps to dictate the overall structure. For example, Pb^{2+} can form a variety of noncentrosymmetric materials with oxygen-containing ligands. Well-known examples that find use as nonlinear optical devices display a diverse range of compositions such as $Pb_{16}(OH)_{16}(NO_3)_{16}$, $Pb_9Te_2O_{13}(OH)(NO_3)_3$, Pb_3SeO_5, and $(Pb_4O)Pb_2B_6O_{14}$.[4−7] Beyond oxide-based ligands, Pb^{2+} halides are finding increased usage as a starting material in the synthesis of newly developed two-dimensional (2D) hybrid perovskites with tunable optical properties. Example materials include $(CH_3NH_3)PbI_3$, $(BZA)_2PbBr_{4-x}Cl_x$, and $(CH_3)_3SPbI_3$,[8−10] where the combination of a lone electron pair on Pb^{2+} and a variety of organic ligands can result in multiple steric configurations. In each of the cases listed above, the complex ligand set around each Pb^{2+} cation dictates the overall structure−property relationships by tuning the chemical bonding environment. This can manifest as changes in the band gap, optical/dielectric response, and polarization. Shifting focus to smaller, model materials that contain Pb^{2+} and only a single anion, such as the solid oxides PbO and $PbCO_3$, these are the starting materials for the commercially important Pb-based functional materials called piezoelectrics and ferroelectrics (such as $PbTiO_3$, $PbZr_{1-x}Ti_xO_3$, and related oxides).[11−13]

While many of the syntheses to form the complex materials in the preceding paragraph take place in conditions that employ elevated temperatures or inert atmosphere, the oxides and carbonates of Pb^{2+} are crucial to a variety of industrial applications where they are in contact with a humid atmosphere or water of varied pH. PbO finds use as a component in TiO_2-supported photocatalysts[14,15] and is an important component in the recycling of Pb-acid battery pastes via aqueous collection methods. $PbCO_3$ is sometimes collected as an insoluble product in this recycling process,[16] which is also capable of multiple conversion/transformation processes. In desulfidization, $PbSO_4$ can be converted in aqueous media to $PbCO_3$ using Na_2CO_3. The rate of this reaction is pH-dependent, influencing the formation of HCO_3^{1-} from CO_3^{2-}.[17] $CaCO_3$ can be converted to $PbCO_3$ in acidic conditions,[18] and it was reported that the highly polarizable Pb^{2+} cation has more acid-stable faces in water than $CaCO_3$ or $SrCO_3$.[19] The transformation properties of $PbCO_3$ also impact human health: it, and more complex solids such as hydrocerussite $Pb_3(OH)_2(CO_3)_2$ and plumbonacrite $Pb_{10}O(OH)_6(CO_3)_6$,[20,21] is found in the corrosion scales of water distribution systems. Adjusting the pH, composition, or treatment procedure of water in contact with these corrosion scales can result in Pb^{2+} release, as exemplified in Washington D.C. (2001−2004)[22−24] and Flint, MI (2014−2017).[25−30] Taken altogether, these examples show that understanding the properties of Pb^{2+} oxides and carbonate surfaces in contact with water, and how to control them, is important to industry

Received: November 17, 2020
Published: January 6, 2021

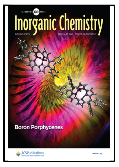

Table 1. For Each Pb and C Species, Tabulated Here Are the pH Range in Which They Are Stable, Followed by ΔG_f^0 and ΔG_2, Both of Which Are Given in Units of eV

species	pH	ΔG_f^0 (eV)	ΔG_2 (eV)
Pb^{+2}	2−6	−0.253	$-2eU_{SHE} + 0.0257 \ln a_{Pb^{+2}} - 0.253$
$PbOH^{+1}$	6−11	−2.345	$-2eU_{SHE} + 0.0257 \ln a_{PbOH^{+1}} - 0.059$ pH + 0.115
$HPbO_2^{-1}$	11−12	−3.507	$-2eU_{SHE} + 0.0257 \ln aHPbO_2^{-1} - 0.177$ pH + 1.413
CO_2	2−6.5	−4.000	$-4eU_{SHE} + 0.0257 \ln a_{CO_2} - 0.236$ pH + 0.920
HCO_3^{-1}	6.5−10.5	−6.081	$-4eU_{SHE} + 0.0257 \ln aHCO_3^{-1} - 0.295$ pH + 1.299
CO_3^{-2}	10.5−12	−5.470	$-4eU_{SHE} + 0.0257 \ln aCO_3^{-2} - 0.354$ pH + 1.910

and human health, in fields that range from functional material design to drinking water treatment.

Prior routes to investigate the properties of Pb-containing solids in contact with water have primarily been experimental,[20,21] and many have relied on speciation relationships derived from stability constants at equilibrium conditions.[31] Pourbaix (speciation) diagrams show that Pb^{2+} is the soluble form of Pb at low pH,[32,33] whereas $PbOH^{1+}$ is preferred for values of pH > 6, but this information does not detail surface processes that could lead to their release in aqueous solutions. Thus far, no models of PbO/$PbCO_3$ surface reactivity, to the best of our knowledge, have incorporated computationally inexpensive methods such as density functional theory (DFT)[34,35] to investigate the initial surface changes that could cause solid decomposition via Pb^{2+} release. DFT methods are ideal for this type of investigation because they allow for a more complete understanding of physical phenomena at the atomistic level. For example, the detailed atomistic information from changes in the surface structure can be linked to computable thermodynamics and distinct features in the electronic structure.

Here, we use DFT to model lead-containing oxides and carbonates, specifically litharge, massicot (α-PbO and β-PbO, respectively), and cerussite ($PbCO_3$). We delineate structure−property relationships for these solid surfaces in contact with water and comment on the initial stages of dissolution via different modes of Pb^{2+} release. Our overall goal is to understand how the properties of surfaces that contain Pb^{2+} change across a wide range of pH, to be able to better inform experiments and applications where Pb^{2+}-based materials are in contact with water. We take a reductionist approach in modeling simple lead oxides and lead carbonates to start. We fully characterize the bulk PbO and $PbCO_3$ and use the bulk structures to create a wide range of Pb-terminated supercell surface slabs. We compute the thermodynamics associated with different surface transformations, focused on the pH-dependent release mechanisms of Pb^{2+} from oxides and carbonate surfaces. For this, we use a DFT + solvent ion model[36−38] that combines quantum mechanically computed total energies (via DFT calculations) with experimentally determined values for changes in the free energy of formation (ΔG_f^0) to create new fundamental insights into the atomistic interactions that dictate surface transformations. Where possible, we link these insights to changes in the electronic structure via projected density of states (PDOS) analyses to better understand the molecular orbital interactions that occur at the surfaces of Pb-based materials.

■ METHODOLOGY

DFT Modeling. The ground-state calculations described here employ periodic DFT methods[34,35] and are carried out using Quantum ESPRESSO, an open source software package.[39] All atoms are represented using GBRV-type ultrasoft pseudopotentials[40,41] and a plane-wave cutoff of 50 Ry. Bulk structural relaxations use a 6 × 6 × 6 k-point grid,[42] and the convergence criterion for self-consistent relaxations was 5×10^{-6} eV. All calculations are performed at the generalized gradient approximation (GGA) level using the Wu−Cohen (WC)-modified PBE-GGA exchange−correlation functional for solids.[43,44] We choose the WC-modified PBE-GGA because of its improved agreement with experimental structures for a wide range of insulators, including oxides,[45] and its ability to well match the properties of known Pb^{2+}-containing oxides such as $PbTiO_3$.[46,47] To demonstrate the improvement in DFT-computed properties of WC over PBE and other exchange−correlation functionals, we include in Section S1 of the Supporting Information a brief discussion and comparison of lattice parameters for select compositions.

To compute the change in free energy of surface transformations (ΔG) of Pb^{2+} solids in contact with water, a DFT + solvent ion method[36,48] is employed. This method is based on Hess's law, where ΔG is partitioned between the computed energies of the reactants and products (used in ΔG_1) and experimental data (used in ΔG_2). Briefly, ΔG_1 is the DFT-computed term that takes into account making and breaking bonds by adding or subtracting neutral atoms to/from the surface. Zero-point energy (ZPE) and $T\Delta S$ correction terms are added to the DFT total energies of supercell surface slabs to obtain ΔG_1, as described in refs 37, 38 and in the style of ref 36. DFT methods can provide reliable trends in the solid state; however, their use in computing the energetics associated with the aqueous redox reactions and variable hydration spheres involved with surface adsorption and release processes is not well defined.[49−51] Therefore, we account for these processes using ΔG_2. This is the term that includes experimentally determined redox and solvation relative to the standard hydrogen electrode.

In this second model term, $\Delta G_2 = \Delta G_{SHE}^0 - n_e eU_{SHE} - 2.303 n_{H^+} kT \text{ pH} + kT \ln a(H_xAO_y)^{z-}$, where ΔG_{SHE}^0 is the change in free energy of each species relative to the standard state, eU_{SHE} is the applied potential, relative to the standard hydrogen electrode, and $a_{H_xAO_y}{}^{z-}$ are the concentrations of the dissolved constituent ions (assumed to be 1×10^{-6} M). n_e and n_{H^+} are the number of electrons and protons involved in the chemical reactions required for surface release. Values of ΔG_f^0, used to compute ΔG_{SHE}^0, and discussed below, are obtained from ref 52. At conditions of $eU_{SHE} = 0$ and $a = 1 \times 10^{-6}$ M, DFT-calculable Pourbaix diagrams[32] show that increasing pH from 2 to 12 changes the preferred aqueous species of Pb from Pb^{+2} to $PbOH^{+1}$ and finally $HPbO_2^{-1}$ and the preferred aqueous species of carbon (C) from CO_2 to HCO_3^{-1} and finally CO_3^{-2}. For this series, we need to add in 1 ΔG_{SHE}^0 (O), which is −2.46 eV, for each oxygen (O) present in the aqueous species to the ΔG_f^0 values obtained from ref 52, in the style of ref 53.

https://dx.doi.org/10.1021/acs.inorgchem.0c03398
Inorg. Chem. 2021, 60, 1228−1240

This transforms each ΔG_f^0 into a ΔG_{SHE}^0 per species, and then it is modified further by including terms related to pH, potential, and concentration. All ΔG_2 values in Table 1 are given relative to O_2 and H_2 gases, which is discussed further in Section S3 of the Supporting Information.

Inspection of Table 1 shows that ΔG_f^0 of Pb^{+2} release is energetically favorable, so ΔG is first computed for the removal of an isolated Pb atom, then its replacement by hydrogen (H) atom(s), and finally for the removal of Pb−OH_n and Pb−CO_3 units per each surface slab. Example reactions are detailed in Section S3 of the Supporting Information.

RESULTS AND DISCUSSION

Bulk Litharge, Massicot, and Cerussite. As shown in Figure 1, both bulk PbO materials have each Pb bound to 4 O and each O is bound to 4 Pb. In each of these structures, a 2D layer-like morphology is present. The stereochemically active lone pair of the Pb repels each other, creating discrete sheets where Pb^{2+} atoms decorate the exterior of each layer so that each PbO is Pb-terminated. In the litharge structure (Figure 1a), the Pb−O layers form flatter sheets than in massicot (Figure 1b), and we compute that the Pb−O bond lengths in litharge are all 2.32 Å. The separation between sheets is 2.66 Å for litharge, which is the vertical distance between Pb atoms. The massicot structure contains corrugated sheets, and we find that the 4 Pb−O bond lengths are 2.24, 2.27, and 2 × 2.46 Å. Massicot has two Pb−O bonds that are shorter and two Pb−O bonds are longer than in litharge. Here, the sheet separation is 3.19 Å, which is 0.5 Å longer than the interplanar separation than in litharge. Table 2 compares the fully relaxed DFT litharge and massicot structures to those found in the Inorganic Crystal Structure Database.[54] The largest deviation between DFT and experiment is the lattice parameter c of massicot, which is underestimated by 0.74%. The bulk primitive unit cell of litharge contains 4 total atoms (2 Pb atoms at Wyckoff position 2c and 2 O atoms at Wyckoff position 2a), and 8 total atoms for massicot (4 Pb atoms and 4 O atoms, each at different Wyckoff positions labeled 4d).

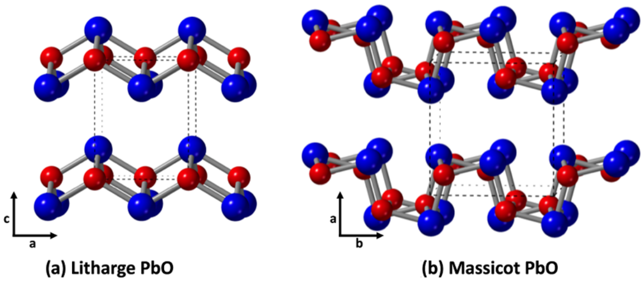

Figure 1. Two bulk PbO crystal structures: (a) tetragonal litharge and (b) orthorhombic massicot. Pb is depicted as a dark blue sphere and O is depicted as a red sphere.

Our DFT-GGA bulk litharge structure was found to have a band gap of 1.16 eV, and massicot has a band gap of 1.97 eV. The corrugated nature of massicot increases the band gap, but Figure 2 shows that both litharge and massicot also have indirect band gaps. In litharge, the valence band maximum (VBM) is near the M-point in the Brillouin zone, and the conduction band minimum (CBM) is found at the Γ-point. In contrast, massicot has a VBM at the Γ-point and a CBM at the R-point. Close inspection of the PDOS of both bulk PbO materials shows similar bonding and antibonding characters. The PDOS of bulk litharge shows that the highest occupied molecular orbitals (HOMOs) are composed mostly of O 2p orbitals mixed with Pb 6s and 6p orbitals, while the lowest unoccupied molecular orbitals (LUMOs) are composed primarily of Pb 6p-orbital character. This ordering of molecular orbitals is also observed in massicot; even though the sheet morphology is different, the tetrahedral bonding environments are similar. These PDOS are consistent with how one would describe the bonding in PbO: O^{2-} is anionic and will be more electronegative, drawing more electron density toward it than the cationic Pb^{2+}. Therefore, the filled O 2s and 2p orbitals will be most of the occupied energy states. The lowest unoccupied states can be explained by the loss of electron density from cationic Pb, which would have lost two electrons from the 6p orbital, and would take less energy to fill than most other orbitals to regain them. The O 2p and Pb 6p orbitals both show delocalized character with wide bandwidth in the PDOS.

Our DFT-GGA-computed crystal structures, PDOS, and electronic band structures of litharge (shown in Figure 2a) are consistent with ref 57 and refs therein that also use similar DFT methodology.

Now, we turn our attention from oxide to carbonate. The crystal structure of bulk cerussite $PbCO_3$ is shown on the left-hand side of Figure 3. Here, each CO_3 unit lies almost horizontally along the z direction, and each Pb is connected to 3 or 4 different CO_3 via Pb−O bonds. These bonds range from 2.60 to 2.72 Å, and each Pb has formed 6−7 bonds to O. The crystal structure of cerussite belongs to the $Pnma$ space group (group 62),[58−60] and a comparison to experimentally determined crystal structures is given in Table 3. All cell angles are 90°, and the largest deviation in lattice constant is the overestimation of a by 0.06 Å. In the cerussite structure, the Pb, C, and O1 are located at Wyckoff positions of symmetry 4d, while O2 is in the Wyckoff position 8d of space group $Pnma$. The $PbCO_3$ primitive unit cell has 20 total atoms, larger than for litharge (4 total atoms) or massicot (8 total atoms). Our DFT-computed crystallographic parameters are

Table 2. Comparison of DFT-Relaxed and Experimentally Determined Crystallographic Parameters of Litharge and Massicot[a]

PbO	a	b	c	Pb(x, y, z)	O(x, y, z)
			Litharge		
DFT	3.989	3.989	5.028	(0.250, 0.250, 0.236)	(0.750, 0.250, 0.000)
exp	3.972	3.972	5.023	(0.250, 0.250, 0.235)	(0.750, 0.250, 0.000)
			Massicot		
DFT	5.900	5.512	4.719	(0.231, 0.011, 0.250)	(0.135, 0.408, 0.250)
exp	5.895	5.493	4.754	(0.230, 0.012, 0.250)	(0.135, 0.408, 0.250)

[a] The Pb and O of the litharge structure are located at Wyckoff positions 2c and 2a, respectively, of space group 129 ($P4/nmm$ symmetry),[55] and in massicot, both are located at 4d positions of space group 57 ($Pbcm$ symmetry).[56]

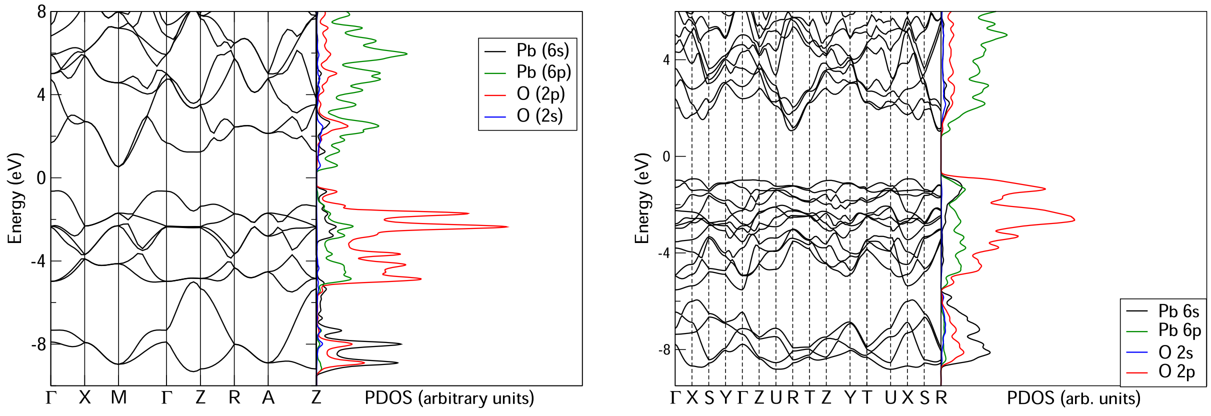

(a) litharge (b) massicot

Figure 2. Electronic band structure and PDOS of (a) litharge and (b) massicot phases of PbO.

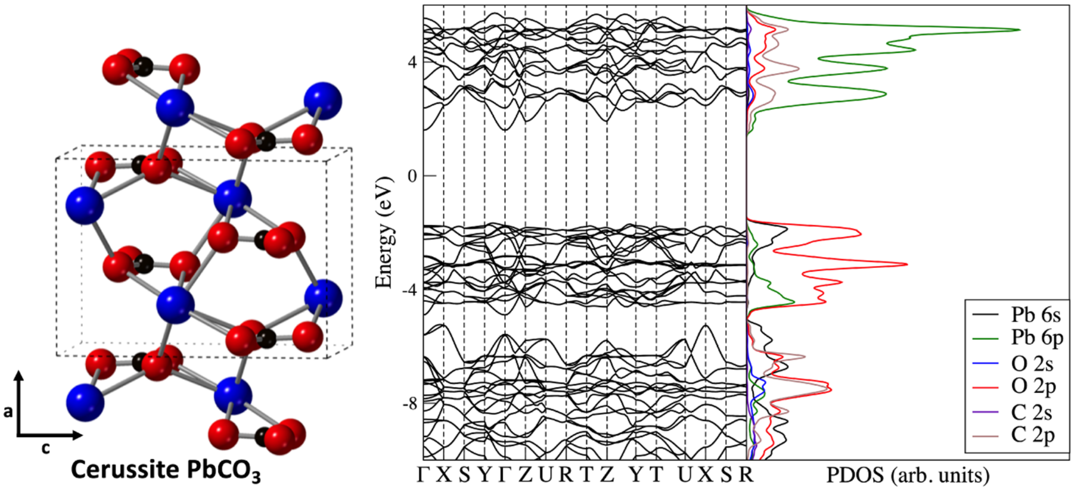

Figure 3. Given on the left-hand side is the structure of orthorhombic $PbCO_3$, cerussite, and on the right-hand side are the electronic band structure and corresponding PDOS. Pb atoms are depicted as dark blue spheres, O atoms as red spheres, and C atoms as black spheres.

Table 3. Comparison of DFT-Relaxed and Experimentally Determined Lattice Constants of Cerussite in the *Pnma* Space Group[a]

$PbCO_3$	*a* (Å)	*b* (Å)	*c* (Å)
DFT	6.073	5.183	8.494
expt	6.134	5.180	8.492

[a] All values are given in units of Angstroms.

Pb (0.245, 0.250, 0.583), C (0.089, 0.250, 0.238), O1 (0.099, 0.250, 0.086), and O2 (0.091, 0.034, 0.315); values close to the experimentally determined crystallographic parameters are Pb (0.245, 0.250, 0.583), C (0.092, 0.250, 0.246), O1 (0.096, 0.250, 0.093), and O2 (0.090, 0.035, 0.314). Unlike the PbO materials in the last section, cerussite does not have Pb-terminated 2D layers but an extended crystal structure.

Bulk cerussite exhibited an indirect band gap of 3.26 eV with both the VBM and CBM lying at, or near, the Γ-point of the Brillouin zone. Our DFT-GGA-computed electronic band structure of cerussite $PbCO_3$ shown in Figure 3 is consistent with entries from the material project (ref 61) using similar methodology. The VBM and CBM are found at or near the same *k*-points in the calculated and reference electronic band structures. Analysis of the PDOS reveals that the occupied states are predominantly composed of O 2p orbitals with additional mixing from Pb 6p and 6s states, as well as C 2p orbitals. This indicates a strong bonding network where each O is bound to multiple cations, and the bonding is more ionic than in either PbO structure. As observed in bulk litharge and massicot, the most significant contribution to the LUMO is made by Pb 6p, but appreciable C 2p-orbital character is noted as a consequence of polar C−O bonds present in the bulk structure. The presence of this bonding character at ≈−6 eV acts as a distinct anion fingerprint that could be used to differentiate complex mixtures in which both O(H) and CO_3(H) anions are present.

Surface Structures and Transformations of PbO and $PbCO_3$. Given the close match between our DFT-calculated bulk structures presented in the last sections, we use each primitive bulk cell to create supercell repeats, which are cleaved to create Pb-terminated surfaces, following the general procedures to create surfaces outlined in refs 37, 62−64. A detailed description of each surface is presented in Section S3 of the Supporting Information. Each of the Pb-containing materials is cleaved along the following planes: litharge is cleaved along the (001) set of planes that intersect with the *z*-axis, massicot is cleaved along the (100) set of planes that intersect with the *x*-axis, and cerussite is cleaved along the

(001) set of planes that intersect with the z-axis. We then vary both (i) the size of repeats in the direction of cleavage and (ii) the in-plane dimensions in an effort to comparatively sample the thermodynamics of surface transformations. For example, in our litharge analysis, we investigate surfaces whose dimensions range from 1 × 1 × 5 (20 atoms) to 2 × 2 × 7 (112 atoms), where the in-plane repeat goes from 1 × 1 to 2 × 2, and the length of the supercell slab length increases from a repeat of 5 PbO units to a repeat of 7. Our range of massicot surfaces is 3 × 1 × 1 (34 atoms) to 5 × 2 × 1 (80 atoms), and for cerussite, it is 1 × 1 × 4 (30 atoms), 1 × 1 × 6 (50 atoms), and 2 × 2 × 4 (120 atoms).

The surfaces and compositions investigated here are not exhaustive but were designed to act as a survey that will be used to develop more refined and complex models in the future. The present work, to the best of our knowledge, is the first study detailing the thermodynamics of surface transformations of Pb^{2+}-containing materials using first-principles DFT, specifically the DFT + solvent ion model.[36] We choose model compositions that are PbO and $PbCO_3$ for simplicity and investigate the release of Pb from PbO and $PbCO_3$ in two ways. The first is through a nonmonotonic surface exchange of Pb and H in Pb-terminated surfaces, and the second is through removal of Pb-anion units, such as $Pb-(OH)_n$ and $Pb-CO_3$, from the hydrated surfaces. These two pathways are illustrated in Figure 4 for litharge surfaces. We use these two modes of release to gain an atomistic understanding of the initial stages of solid dissolution and acknowledge that there could be other mechanisms in which Pb could be released in aqueous environments.

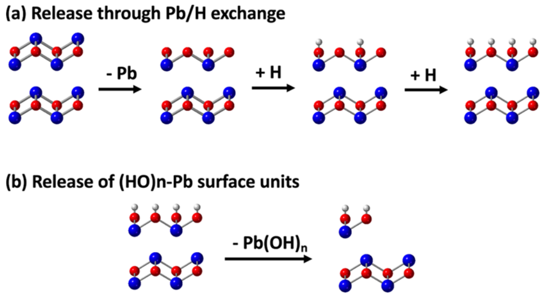

Figure 4. Two surface release pathways of Pb studied here include (a) Pb/H exchange and (b) Pb-anion removal, shown here for litharge as $Pb(OH)_n$. Color scheme is as in previous figures, and H atoms are represented as white spheres.

We now turn our comparative analysis to the electronic structure and PDOS of litharge PbO supercell surfaces, specifically investigating the difference between Pb- and H-terminated surfaces, where the H-terminated surfaces are the result of the surface exchange depicted on top of Figure 4.

When the bulk litharge structure is expanded to create the Pb-terminated surface, all of the major peaks in the PDOS (in Figure 5a) remain consistent with the bulk structure. O 2p-orbital character still dominates the HOMO, and the LUMO is mostly Pb 6p orbitals, as shown in the bulk structures in Figure 2a. When the terminal Pb of the litharge surface is replaced with 2H atoms, in these surfaces we create strong O−H surface bonds, where the Pb and H are found in crystallographically distinct locations. The exchange of Pb for 2H results in few changes to the PDOS. On comparing Figure 5a,b, there is a new O 2p-orbital peak around −7.5 eV, and it lines up with the peak of the H 1s orbital, so it is likely the energy of the bond between the O and H atoms. The band gap also increased from 1.31 to 1.42 eV after exchanging the terminal surface atoms, both of which are larger than the bulk value of 1.16 eV. The increase in band gap can be explained by the more ionic interaction that O has with H when compared to that with Pb. The interaction of H and O is more ionic in character than that of the Pb−O bond, increasing the overall strength and creating surface dipoles. The massicot PDOS (Figure S1 in Section S4 of the Supporting Information) showed similar changes to litharge. An overlapping peak of O 2p, H 1s, and Pb is present at −7 eV. This peak is analogous to the peak around −7.5 eV of the H-terminated litharge surface. Additionally, the massicot electrons became much more localized when the surface is H-terminated with four seemingly distinct peaks when compared to the Pb-terminated surface with two broad peaks. The PDOS of different PbO surfaces yield telltale signs of how changes in the chemical environment can manifest as distinct features in the electronic structure.

After characterizing the electronic structure of the PbO surfaces and identifying potential bonding and antibonding interactions that could serve as fingerprint regions for more

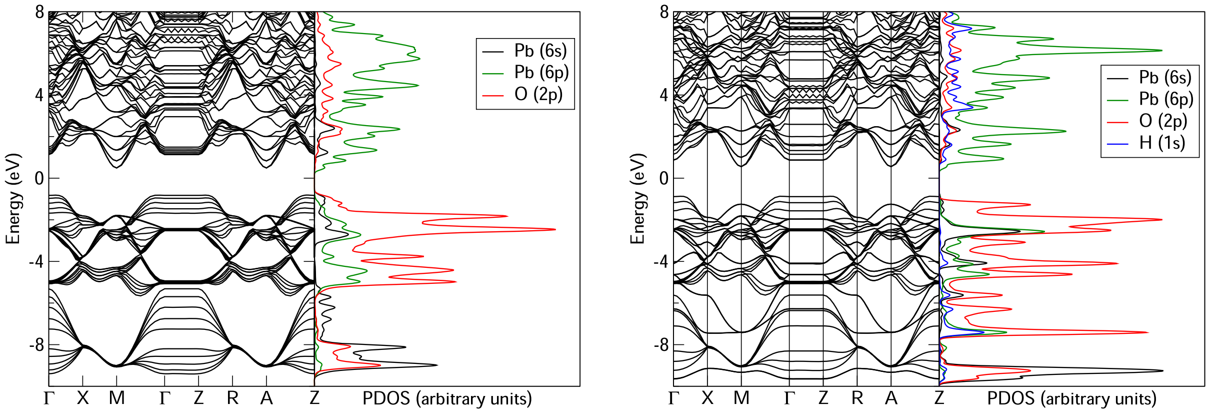

(a) Pb-terminated (b) H-terminated

Figure 5. Compared here are the electronic structure and PDOS of 1 × 1 × 7 litharge supercell surfaces that are terminated with (a) Pb and (b) H, where each surface Pb was exchanged for 2H.

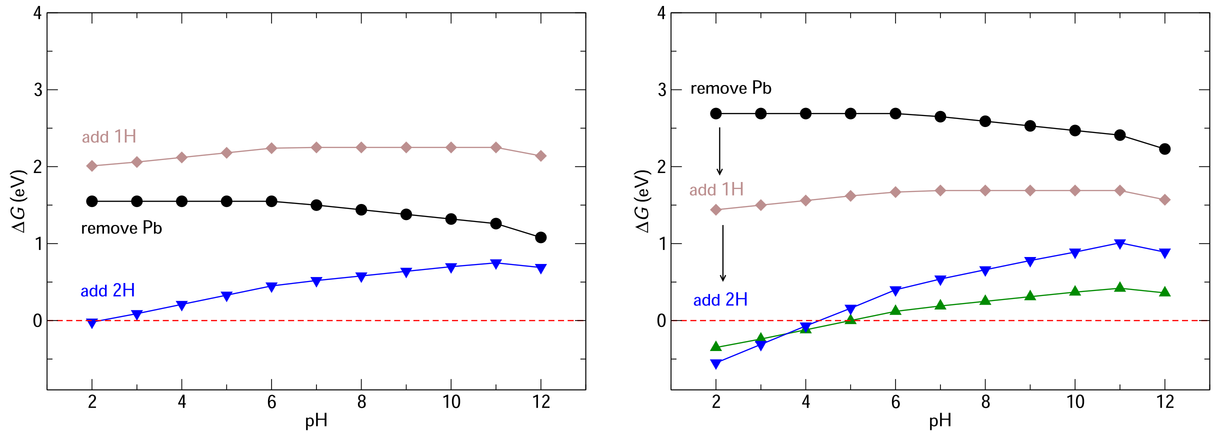

(a) Litharge (b) Massicot

Figure 6. Depicted here are plots of ΔG vs pH for (a) $1 \times 1 \times 5$ litharge and (b) $3 \times 1 \times 1$ massicot supercells, respectively. The black trend line is for removing a Pb atom, the brown trend line for replacing it with 1 H atom, and the blue and green lines are for replacing the Pb with 2H atoms. In this example, there are two different surface configurations of 2H terminated massicot. The dashed red line is at $\Delta G = 0$ crossover point between $\Delta G > 0$ (unfavored) and $\Delta G < 0$ (favored). All values of ΔG are given in units of eV.

complex mixtures, we turn to a comparison of the thermodynamics of surface exchange for the smallest supercells of PbO. Each step of the surface exchange, pictured in Figure 4, is shown in Figure 6, which depicts how ΔG changes as a function of pH for (a) litharge and (b) massicot as atoms are removed or added. The first step, removing a terminal Pb atom by itself, from either the PbO surface has all values of $\Delta G > 0$ for the entire range of pH depicted (black trend lines). The range of values here is ≈1−1.5 eV for litharge and ≈2−2.5 eV for massicot and corresponding to 100 and 50% surface Pb removal, respectively. The ΔG values are twice as large for massicot because of the additional surface reconstructions that take place; surface O becomes subsurface O, where the corrugated nature of the bonds readjusts to accommodate the underbound surface O. This surface is then partially charge-compensated in the second step when 1 H is added to create a strong polar OH surface bond (brown trend line). In the final step, the surface is fully charge-compensated when another H atom is added to generate a fully H-terminated surface (blue/green trend lines). The overall effect in both PbO structures is that exchanging 1 Pb for 2H atoms results in the lowest ΔG of the sets of transformations investigated here, but that does not mean that the exchange process is favored for the entire range of pH in Figure 6. For the smallest supercells in our set, the Pb/2H exchange is predicted to be favorable at pH values below 2.19 and 4.26 for litharge and massicot, respectively. We interpret this to mean that if a Pb atom is exposed at the surface, in either the litharge or massicot geometries, then it will be a stable surface atom for pH values greater than 5, barring any external interactions, which may include other cations (Al, Fe, Mn, etc.)[65,66] or anions (chloride (Cl), phosphate, sulfates, etc.).[20,31,67,68] We report the values of ΔG_1 and ΔG_2 (at 3 different pH) used to create Figure 6 in Table 4, as well as the range of other supercells studied here.

Table 4. Tabulated Here Are the ΔG_1 and ΔG_2 Values for Varied Supercells of the Litharge and Massicot Phases of PbO[a]

litharge	process	ΔG_1 (eV)	$\Delta G_2^{\text{pH 3}}$ (eV)	$\Delta G_2^{\text{pH 7}}$ (eV)	$\Delta G_2^{\text{pH 11}}$ (eV)
1 × 1 × 5	r1Pb	2.15	−0.61	−0.65	−0.89
	r1Pb-a1H	2.50	−0.43	−0.24	−0.24
	r1Pb-a2H	0.35	−0.25	0.17	0.41
	rPb(OH)$_2$	5.81	−5.17	−4.75	−4.51
1 × 1 × 7	r1Pb-a2H	0.35	−0.25	0.17	0.41
	rPb(OH)$_2$	5.80	−5.17	−4.75	−4.51
2 × 1 × 7	r2Pb-a4H	−0.33	−0.51	0.34	0.81
	rPb(OH)$_2$	7.27	−5.17	−4.75	−4.51
2 × 2 × 7	r4Pb-a8H	−0.65	−1.02	0.69	1.63
	rPb(OH)$_2$	7.33	−5.17	−4.75	−4.51
massicot	process	ΔG_1 (eV)	$\Delta G_2^{\text{pH 3}}$ (eV)	$\Delta G_2^{\text{pH 7}}$ (eV)	$\Delta G_2^{\text{pH 11}}$ (eV)
3 × 1 × 1	r1Pb	3.30	−0.61	−0.65	−0.89
	r1Pb-a1H	1.93	−0.43	−0.24	−0.24
	r1Pb-a2H	0.02	−0.25	0.17	0.41
	r2Pb-a4H	0.20	−0.51	0.34	0.81
	rPb(OH)$_2$	7.09	−5.17	−4.75	−4.51
5 × 2 × 1	r1Pb	13.31	−0.61	−0.65	−0.89
	r1Pb-a1H	6.89	−0.43	−0.24	−0.24
	r1Pb-a2H	0.40	−0.25	−0.17	0.41
	rPb(OH)$_2$	8.18	−5.17	−4.75	−4.51
	r4Pb-a8H	−1.03	−1.02	0.69	1.63
	rPb(OH)$_2$	7.15	−5.17	−4.75	−4.51
	rPb(OH)$_3$	11.52	−7.46	−6.79	−6.32
	rPb$_2$(OH)$_2$	12.41	−8.07	−7.45	−7.22

[a] Lowercase "r" stands for removal and lowercase "a" stands for addition. For example, the entry "r1Pb-a1H" means the removal of 1 Pb and addition of 1 H. The ΔG_2 values are given for pH 3, pH 7, and pH 11 to compare the relative change in thermodynamics at acidic, neutral, and basic pH. All values are reported in units of eV.

While the DFT + solvent ion method allows us to partition the errors inherent to DFT from the errors inherent to thermodynamics experiments, it also allows us to partition the free energies required to make and break bonds from the free energies associated with solvation. This affords us a separable analysis of the components of ΔG. Inspection of Table 4 shows that (i) the predicted favorability of some reactions depends upon the supercell size (Pb/H surface exchange) while some processes (ii) will rarely be favorable (removal of surface Pb(OH)$_2$ units). To illustrate the first point, we focus on the full Pb/H exchange of two different litharge supercells. Summing the ΔG_1 of exchanging 1 Pb/2H for the 1 × 1 ×

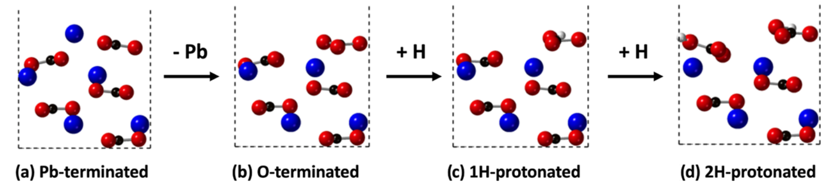

Figure 7. DFT-computed structures for each step of the surface exchange of Pb and H for a $PbCO_3$ surface slab, whose ΔG values are plotted in Figure 9.

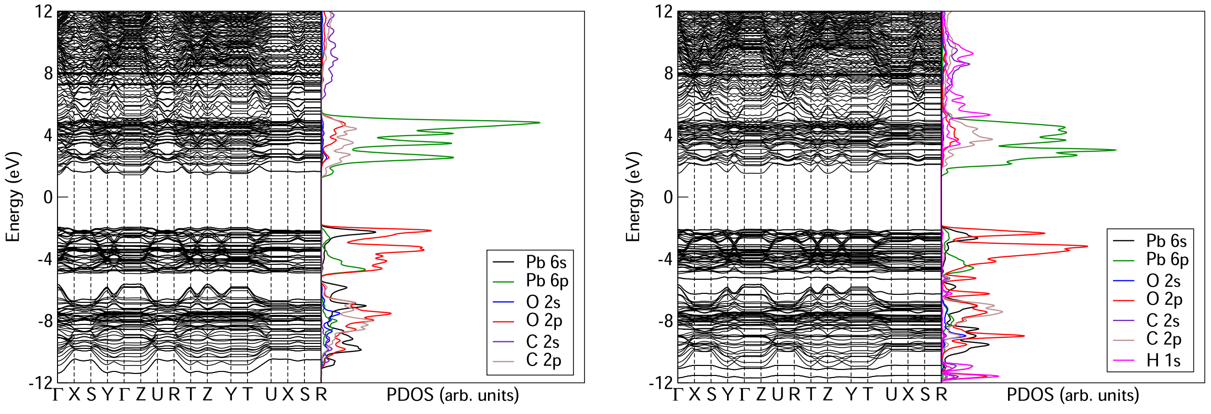

(a) Pb-terminated (b) H-terminated

Figure 8. Electronic band structure and corresponding PDOS for (a) Pb- and (b) H-terminated 1 × 1 × 6 $PbCO_3$ surfaces.

5 supercell (the process row labeled "r1Pb-a2H") and ΔG_2 at pH 3 yields +0.10 eV, which is not predicted to be favorable. Summing the ΔG_1 of exchanging 2 Pb/4H for the 2 × 1 × 7 supercell (the process row labeled "r2Pb-a4H") and ΔG_1 at pH 3 yields −0.84 eV, which is predicted to be favorable. The more surface exchanges are present, the more likely the process will occur because it is energetically preferable to release multiple Pb to solution as Pb^{2+} and form many strong OH bonds. Attending to the second point, all ΔG_1 values of removing $Pb(OH)_2$ units from massicot (labeled "r$Pb(OH)_2$" in the bottom half of Table 4) are larger than +7 eV, while ΔG_2 values at acidic pH are ≈−5 eV. The favorable release of ions into solution is not large enough to compensate for the number of bonds broken to release a $Pb(OH)_2$ unit, even at low pH. This means that under the conditions explored here, only the surface exchange of Pb and H is preferable for litharge and massicot.

After the PDOS and thermodynamics analysis of litharge and massicot, we now investigate surfaces that contain the CO_3 anion, cerussite phase $PbCO_3$. A depiction of the surface exchange process for cerussite is shown in Figure 7. One of the biggest differences between PbO and $PbCO_3$ is that each Pb is bound to 6−7 O atoms, spread across multiple carbonate units in all three Cartesian directions, while in PbO each Pb was bound to 4 O atoms in a tetrahedral array. In the Pb/H surface exchange along the (001) direction of $PbCO_3$, the soluble HCO_3 anion is formed, and this changed the orientation of the CO_3 units relative to their bulk and/or Pb-terminated surface positions. As much as 50% of the HCO_3 surface units go from a completely horizontal orientation to an orientation with a vertical component where some C−O surface atoms have displaced as far as ≈0.7−0.9 Å. The differences in electronic states between the Pb- and H-terminated $PbCO_3$ surfaces are depicted in Figure 8.

In the $PbCO_3$ surface PDOS, the Pb-terminated surface (Figure 8a) retained most of the characteristic peaks found in both the occupied and unoccupied states of the bulk structure. The orbital distribution is not significantly affected in the bulk-to-surface transformation other than the occurrence of charge localization in both the HOMO and LUMO. Pb 6p-orbital character remains predominant in the LUMO as does O 2p-orbital character in the HOMO. Overall, no significant changes in bond or orbital composition were observed in the expansion of bulk cerussite to the Pb-terminated supercell surface. In the transformation of the Pb-terminated surface to a H-terminated surface via Pb/H exchange (Figure 8b), an increase in band gap from 3.38 to 3.61 eV was measured, suggesting a strong bonding network and possibly greater ionic bond composition within the hydrogen-terminated surface. As observed in PbO, these values are both higher than the bulk band gap computed for cerussite, 3.26 eV. Augmentation of the occupied states was mostly limited to the appearance of two additional peaks near −10 eV, corresponding to mixing of C 2s, C 2p, and O 2p states with H 1s, as well as notable localization of O 2p states between −4 and −6 eV. This is most likely the bonding states of CO_3 anion. The bandwidth of the unoccupied states of the hydrogen-terminated surface increased by 1.5 eV, and a substantial amount of mixing from H 1s was observed, suggesting a significant amount of O−H bonding with partial ionic composition. Extensive overlap of H 1s with C 2s was also present in the LUMO, suggesting the presence of residual C−H bonding, which is further corroborated by H 1s overlap with C 2s and 2p in the lower occupied states at −10 eV. The differentiation in bonding between CO_3 and HCO_3 anion units is a key fingerprint in the electronic structure analysis.

The thermodynamics of each step of the Pb/H surface exchange for a 1 × 1 × 5 $PbCO_3$ supercell is plotted in Figure 9. We predict similar trends to the stepwise mechanistic

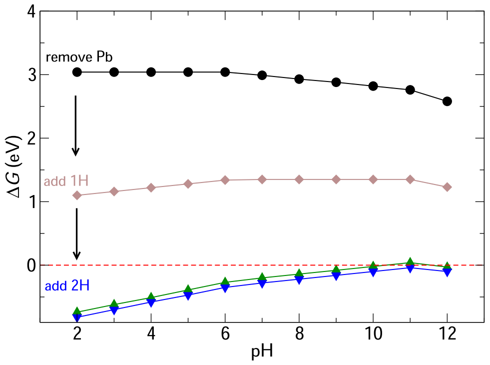

Figure 9. ΔG as a function of pH for each step of the Pb/2H surface exchange of a 1 × 1 × 6 $PbCO_3$ supercell. The blue and green trend lines are for two different configurations of H additions.

interactions shown in Figure 6 for litharge and massicot. Removal of a Pb atom from a Pb-terminated surface is highly unfavored: $\Delta G > 0$ for the entire range of pH values depicted here. The successive addition of H atoms to the surface creates HCO_3 anions, and this surface exchange of H for Pb is favorable for a much wider pH range than observed in PbO. Even varying the distance between the 2H atoms yields similar values of ΔG, and this is depicted as the blue and green trend lines in Figure 9.

We interpret this as the exchange of the exposed surface Pb with 2H is favorable for the entire range of pH investigated here, and as enumerated in Table 5, it is the case for all Pb/2H exchanges up to pH 11. The implication of this result is that in aqueous environments where $PbCO_3$-based structures (such as cerussite and hydrocerussite) are found, then any exposed Pb atoms will be released and replaced by H atoms.

Table 5. Tabulated Here Are the ΔG_1 and ΔG_2 Values for Varied Supercells of $PbCO_3$[a]

cerussite	process	ΔG_1 (eV)	$\Delta G_2^{\text{pH 3}}$ (eV)	$\Delta G_2^{\text{pH 7}}$ (eV)	$\Delta G_2^{\text{pH 11}}$ (eV)
1 × 1 × 6	r1Pb	3.65	−0.61	−0.65	−0.89
	r1Pb-a1H	1.59	−0.43	−0.24	−0.24
	r1Pb-a2Ha	−0.54	−0.25	0.17	0.41
	r1Pb-a2Hb	−0.37	−0.25	0.17	0.41
	$rHCO_3$	10.99	−6.64	−6.44	−6.48
	$rPbHCO_3$	11.71	−7.24	−7.06	−7.06
2 × 1 × 6	r1Pb	3.55	−0.61	−0.65	−0.89
	r1Pb-a1H	1.49	−0.43	−0.24	−0.24
	r1Pb-a2Ha	−0.50	−0.25	0.17	0.41
	r1Pb-a2Hb	−0.39	−0.25	0.17	0.41
	r2Pb-a4Hb	−0.37	−0.51	0.34	0.81
	$rHCO_3$	11.16	−6.64	−6.44	−6.48
	$rPbHCO_3$	12.15	−7.24	−7.06	−7.06
2 × 2 × 4	r1Pb	3.57	−0.61	−0.65	−0.89
	r1Pb-a1H	1.45	−0.43	−0.24	−0.24
	r1Pb-a2Ha	−0.35	−0.25	0.17	0.41
	r1Pb-a2Hb	−0.48	−0.25	0.17	0.41
	r4Pb-a8H	−1.37	−1.02	0.69	1.62
	$rHCO_3$	11.13	−6.64	−6.44	−6.48
	$rPbHCO_3$	12.60	−7.24	−7.06	−7.06

[a] The ΔG_2 values are given for pH 3, pH 7, and pH 11 to compare the relative change in thermodynamics at acidic, neutral, and basic pH. All ΔG_1 and ΔG_2 values are reported in units of eV.

Given this result, we go on to compute the thermodynamics of subsequent Pb release from a H-terminated surface. We obtain ΔG values of releasing HCO_3 and $PbHCO_3$ units from all 3 $PbCO_3$ supercells listed in Table 5. Removing a HCO_3 unit has ΔG_1 ranges from 10.99 to 11.16 eV, and the smallest ΔG_2 at low pH in our set is −6.64 eV. This means that the energetically favorable release of HCO_3 to the aqueous solution cannot compensate for the number and types of bonds that need to be broken by its release; the release is energetically unfavorable (overall $\Delta G > 0$). Coupling a Pb atom release to HCO_3 increases the range of ΔG_1 values to 11.71−12.60 eV, while the gain in releasing Pb to solution only drives ΔG_2 down by ≈0.6 eV. This release is also predicted to not occur, barring any other interactions with cations and anions, which were not taken into account here. In brief, only the exchange of Pb and H atoms at the surface of $PbCO_3$ is found to be energetically favorable.

Comparison of Surface Transformation Thermodynamics. The trends presented in the previous sections allow for a comparison of the free-energy changes involved in making and breaking surface bonds, for a wide variety of chemical environments, involved in Pb release in aqueous media. Using the DFT + solvent ion model, we are able to correlate perturbations and local changes at the atomistic level to the electronic structure and thermodynamics associated with surface transformations of Pb oxides and carbonates.

A comparison of the ΔG_1 values for different processes yields insights into the energetics of making and breaking surface bonds in PbO and $PbCO_3$. Tables 4 and 5 show that removing surface Pb atoms (r1Pb), without creating OH bonds by exchanging Pb with H, is ≈+2−4 eV, where the free-energy penalty for Pb atom removal from litharge (2.15 eV) is less than for massicot (3.30 eV) and cerussite (3.65 eV). This trend reverses as protonation begins. Compensating the surfaces where Pb atoms have been removed with 1 H still costs about ≈1−3 eV, where the overall ΔG_1 values are 1.49−1.59 eV for $PbCO_3$, 1.93 eV for massicot, and 2.50 eV for litharge. This means that the addition of H atoms to create HCO_3 units at the surface of $PbCO_3$ is energetically more preferred than creating OH units at the surface of PbO.

When compensating surfaces by exchanging 2H atoms for 1 Pb atom (to create a charge-neutral surface), the ΔG_1 values from Tables 4 and 5 range from ≈−0.5 to 0.5 eV. Our range of values for a single Pb/2H exchange is −0.54 to −0.37 eV for cerussite, −0.65−0.35 eV for litharge, and 0.02−0.40 eV for massicot, where only cerussite has all $\Delta G_1 < 0$ for the rPb-a2H-type exchange. Considering instead the full exchange of a supercell surface, where all Pb atoms are removed and replaced by 2H atoms, this process varies with the total number of exchanges. The values of ΔG_1 change with increasing number of atoms, and we find that the range of ΔG_1 values for cerussite is −0.54 (r1Pb-a2H) to −1.37 eV (r4Pb-a8H), is 0.20 (r2Pb-a4H) to −1.03 eV (r4Pb-a8H) for massicot, and is 0.35 (r1Pb-a2H) to −0.65 eV (r4Pb-a8H) for litharge. It is these values, when combined with the pH-dependent ΔG_2, that are used to generate the plots in Figure 10. As we vary the dimensions of the PbO and $PbCO_3$ supercells, the pH at which the $\Delta G = 0$ is crossed will change, and we interpret this as the pH at which the exchange process is predicted to occur. Figure 10 shows that the exposed surface Pb atoms will be replaced by 2H at pH values as high as 6.89 for litharge, 8.46 for massicot, and 10.29 for cerussite, depending upon the size of the supercell repeat, and that this is a possible release mechanism for Pb.

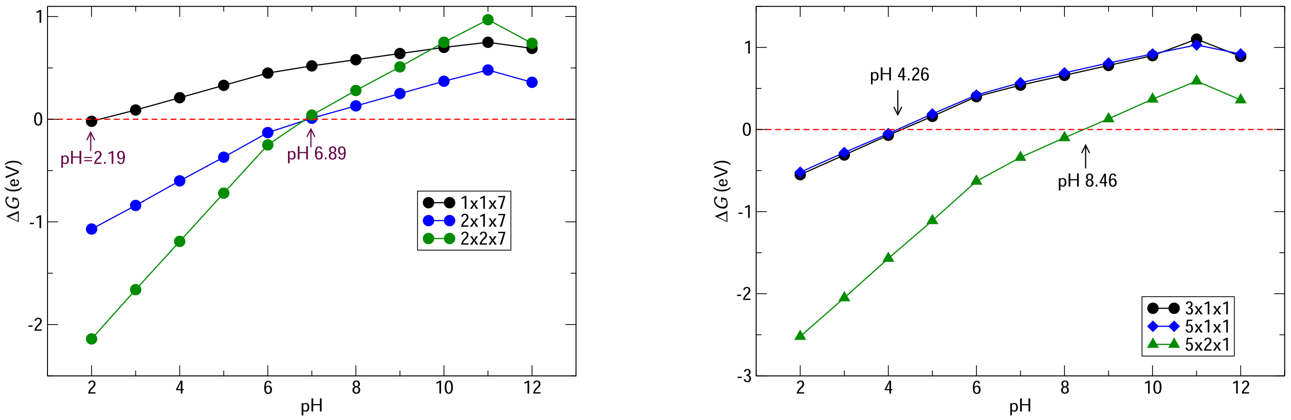

(a) Litharge (b) Massicot

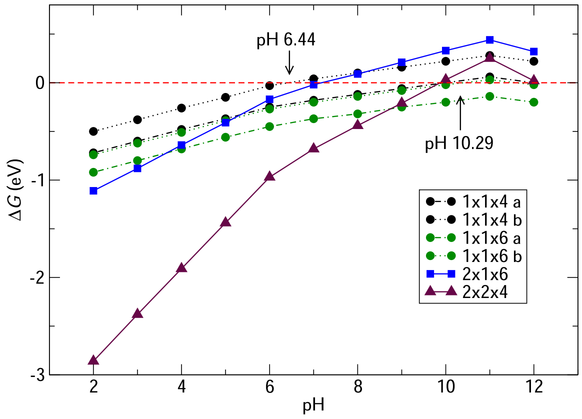

(c) Cerussite

Figure 10. ΔG vs pH for full Pb/H surface exchanges is shown here for (a) litharge, (b) massicot, and (c) cerussite. Each figure also shows the range of pH values for which ΔG = 0 is predicted to change as the size of the supercell increases.

Another route to Pb release could be the release from a protonated surface. To investigate this, we created a series of single $Pb(OH)_n$ vacancies in litharge (and massicot) and found that ΔG_1 was always more than 5 eV (and always over 7 eV) at Pb surface vacancy densities of 50% or less. For litharge, our ΔG_1 values were 5.80 (100%), 7.27 (50%), and 7.33 eV (25%), and for massicot, they were 7.09 (50%) and 7.15 eV (25%), where the number in parentheses is the fractional density of Pb atoms released. We also computed the change in free energy of removing HCO_3 and $PbHCO_3$ from a fully protonated surface, and the ranges of ΔG are 10.99−11.16 and 11.71−12.16 eV, respectively. Removing $PbHCO_3$ is ≈1 eV more costly than removing only HCO_3: anion-assisted release is more favorable than releasing the atom on its own but not as favorable as exchange with 2 protons.

We can take each of the DFT-computed ΔG_1 values and combine them with ΔG_2 values (at each pH) to compute the overall ΔG of each $Pb(OH)_n$ and $PbHCO_3$ release cycle. The favorable change in free energy to release ions to solution, approximated here as ΔG_2, is not enough to compensate for the change in free energy of breaking bonds at the surface, even at very low pH, to release Pb in the forms of $Pb(OH)_n$ or $PbHCO_3$. In Tables 4 and 5, the ΔG_2 values of species, where O-containing anions are released, do decrease with successive addition of O but are rarely enough to compensate for the type and number of Pb−O bonds that need to be broken for the species to be released. We find this to be true for the range of Pb vacancy configurations studied here, from 25 to 100%, for the representative set of surfaces. This means that in our evaluation, only the surface exchange of exposed Pb atoms for multiple H atoms is favorable for specific ranges of pH and that this exchange is dependent upon the chemical bonding environments of the different Pb oxides and carbonates. Any further subsurface release of $Pb(OH)_n$ and $PbHCO_3$ from fully protonated surfaces is predicted to be unfavorable for most configurations studied here.

■ CONCLUSIONS

Collectively, our preliminary analyses of Pb^{2+}-containing oxides and carbonates demonstrate that if the exposed surface Pb is not shielded, then we predict that it will exchange with H and that this process is dependent upon the chemical environment of the Pb atom. Our detailed range of structures shows that this surface exchange can happen at pH values even as high as 10.29 ($PbCO_3$) and that the release of Pb is highly reliant upon its coordination environment and pH. We have developed a quantitative guide for linking changes in surface structure to calculable thermodynamics and can build upon the preliminary work here to include more complex Pb materials such as hydrocerussite $Pb_3(OH)_2(CO_3)_2$ and plumbonacrite $Pb_{10}O(OH)_6(CO_3)_6$[20] and better inform the synthesis of nonlinear optical materials and ferroelectrics that include Pb^{2+}. Moreover, the models presented here could be applied to delineate structure−property trends of Pb-containing 2D hybrid perovskites in contact with water or a humid environment to protect them against potential routes of decomposition.

Our modeling efforts yield atomistic insights into the surface transformations of Pb-based materials in aquatic conditions and can be used to better understand how different nanomaterials react across a wide variety of chemical environments. The reductionist approach taken here complements prior investigations into the reactivity of ZnO, TiO_2, and Ag nanoparticles[69−73] and, more recently, complex metal oxides[38,74−76] of varying dimensionality. The PbO structures here are 2D sheets, and $PbCO_3$ is an extended bonding network, and we predict that both will release Pb atoms under different pH conditions. The release of surface Pb in exchange for H atoms tracks inversely with coordination environment: the fewer, closer Pb−O bonds in litharge require a lower pH to release surface Pb than in cerussite, with more Pb−O bonds. We also find that the subsequent release of Pb and corresponding anions (OH vs HCO_3) from a surface that has already undergone Pb/H exchange tracks with the size of band gap. It is more difficult to release subsurface Pb with a HCO_3 unit than it is an OH unit because more ionic bonds need to be broken in cerussite than in litharge or massicot. This implies that one would need solution additives to control the aqueous reactions of Pb-based materials beyond varying the pH of solution. For example, enhanced dissolution to release Pb would require the addition of chelating agents and the addition of pH buffers to modify the rate of formation of HCO_3.

Additional complexities that could extend the studies here, using the DFT + solvent ion model, could be the inclusion of Pb^{4+} oxide surfaces, complex phosphate−surface interactions,[77,78] and the addition of corrosive agents like chloride (Cl).[21,79] The addition of corrosive interactions via adsorbates containing Cl would be of interest in communities where increased road salt has led to increased pipe pitting and excessive galvanic corrosion of drinking water distribution systems.[80,81] The methodology and surface release trends developed here could also be applied to the field of environmental chemistry, where Pb^{2+} adsorption and release on hydrated Fe and Al-(hydr)oxides[82−85] could be investigated by varying both the pH and concentration terms in the ΔG_2 term, complemented prior research on mineral surface reactivity.[53] Finally, another route to showcase the versatility of the DFT + solvent ion model that incorporates data generated here would be a readily computable, detailed mechanistic understanding of substitution and conversion reactions, specifically the formation of $PbCO_3$ from $PbSO_4$ or from $SrCO_3$, where in each case, either the anion or cation is exchanged.

■ ASSOCIATED CONTENT

Supporting Information

The Supporting Information is available free of charge at https://pubs.acs.org/doi/10.1021/acs.inorgchem.0c03398.

Exchange−correlation functional comparisons, surface calculation details, DFT + thermodynamics calculation details, and assorted PDOS comparisons (PDF)

■ AUTHOR INFORMATION

Corresponding Author

Joseph W. Bennett − *Department of Chemistry and Biochemistry, University of Maryland, Baltimore County, Baltimore, Maryland 21250, United States;* orcid.org/0000-0002-7971-4772; Email: bennettj@umbc.edu

Authors

Ryan T. Grimes − *Department of Chemistry and Biochemistry, University of Maryland, Baltimore County, Baltimore, Maryland 21250, United States*

Joshua A. Leginze − *Department of Chemistry and Biochemistry, University of Maryland, Baltimore County, Baltimore, Maryland 21250, United States*

Robert Zochowski − *Department of Chemistry and Biochemistry, University of Maryland, Baltimore County, Baltimore, Maryland 21250, United States*

Complete contact information is available at: https://pubs.acs.org/10.1021/acs.inorgchem.0c03398

Notes

The authors declare no competing financial interest.

■ ACKNOWLEDGMENTS

J.W.B. acknowledges funding from the Middendorf Foundation and resources provided by the College of Natural and Mathematical Sciences and the Department of Chemistry and Biochemistry at the University of Maryland, Baltimore County. This work used the Extreme Science and Engineering Discovery Environment (XSEDE[86]), which is supported by National Science Foundation grant number ACI-1548562 through allocation ID TG-CHE190075. The hardware used in some of the computational studies is part of the UMBC High Performance Computing Facility (HPCF). The facility is supported by the U.S. National Science Foundation through the MRI program (grant nos. CNS-0821258, CNS-1228778, and OAC-1726023) and the SCREMS program (grant no. DMS-0821311), with additional substantial support from the University of Maryland, Baltimore County (UMBC).

■ REFERENCES

(1) Walsh, A.; Watson, G. W. The origin of the stereochemically active Pb(II) lone pair: DFT calculations on PbO and PbS. *J. Solid State Chem.* **2005**, *178*, 1422−1428.

(2) Payne, D.; Egdell, R. G.; Walsh, A.; Watson, G. W.; Guo, J.; Glans, P. A.; Learmonth, T.; Smith, K. E. Electronic origins of structural distortions in post-transition metal oxides: Experimental and theoretical evidence for a revision of the lone pair model. *Phys. Rev. Lett.* **2006**, *96*, No. 157403.

(3) Payne, D.; Egdell, R. G.; Law, D.; Glans, P. A.; Learmonth, T.; Guo, K. E. S. J.; Walsh, A.; Watson, G. W. Experimental and theoretical study of the electronic structures of α-PbO and β-PbO_2. *Phys. Rev. Lett.* **2006**, *96*, No. 157403.

(4) Chang, L.; Wang, L.; Su, X.; Pan, S.; Hailili, R.; Yu, H.; Yang, Z. A Nitrate Nonlinear Optical Crystal $Pb_{16}(OH)_{16}(NO_3)_{16}$ with a Large Second-Harmonic Generation Response. *Inorg. Chem.* **2014**, *53*, 3320−3325.

(5) Chen, Y.-G.; Yang, N.; Jiang, X.-X.; Guo, Y.; Zhang, X.-M. Pb@Pb_8 Basket-Like-Cluster-Based Lead Tellurate-Nitrate Kleinman

Forbidden Nonlinear Optical Crystal: $Pb_9Te_2O_{13}(OH)(NO_3)_3$. *Inorg. Chem.* **2017**, *56*, 7900−7906.

(6) Kim, S.-H.; Yeon, J.; Halasyamani, P. S. Noncentrosymmetric Polar Oxide Material, Pb_3SeO_5: Synthesis, Characterization, Electronic. *Chem. Mater.* **2009**, *21*, 5335−5342.

(7) Zhang, F.; Zhang, F.; Lei, B.-H.; Yang, Z.; Pan, S. Synthesis, Characterization, and Theoretical Studies of $(Pb_4O)Pb_2B_6O_{14}$: A New Lead(II) Borate with Isolated Oxygen-Centered Pb_4O Tetrahedra and Large Second Harmonic Generation Response. *J. Phys. Chem. C.* **2016**, *120*, 12757−12764.

(8) Stoumpos, C. C.; Malliakas, C. D.; Kanatzidis, M. G. Semiconducting Tin and Lead Iodide Perovskites with Organic Cations: Phase Transitions, High Mobilities, and Near-Infrared Photoluminescent Properties. *Inorg. Chem.* **2013**, *52*, 9019−9038.

(9) MH, J. White-Light Emission from the Structural Distortion Induced by Control of Halide Composition of Two-Dimensional Perovskites ($(C_6H_5NH_3)_2PbBr_{4-x}Cl_x$). *Inorg. Chem.* **2019**, *58*, 6748−6757.

(10) Kaltzoglou, A.; Stoumpos, C. C.; Kontos, A. G.; Manolis, G. K.; Papadopoulos, K.; Papadokostaki, K. G.; Psycharis, V.; Tang, C. C.; Jung, Y.-K.; Walsh, A.; Kanatzidis, M. G.; Falaras, P. Trimethylsulfonium Lead Triiodide: An Air-Stable Hybrid Halide Perovskite. *Inorg. Chem.* **2017**, *56*, 6302−6309.

(11) Berbenni, V.; Milanese, C.; Marini, A.; Welham, N. J. Effect of Mechanical Activation on the Formation of Lead Titanates from $PbCO_3$-TiO_2 Mixtures. *J. Mater. Sci.* **2006**, *41*, 1739−1744.

(12) Cai, Z.; Xing, X.; Yu, R.; Sun, X.; Liu, G. Morphology-Controlled Synthesis of Lead Titanate Powders. *Inorg. Chem.* **2007**, *46*, 7423−7427.

(13) Denis Romero, F. D.; Patino, M. A.; Haruta, M.; Kurata, H.; Attfield, J. P.; Shimakawa, Y. Conversion of a Defect Pyrochlore into a Double Perovskite via High-Pressure, High-Temperature Reduction of Te^{6+}. *Inorg. Chem.* **2020**, *59*, 343−349.

(14) Bhachu, D. S.; Sathasivam, S.; Carmalt, C. J.; Parkin, I. P. PbO-Modified TiO_2 Thin Films: A Route to Visible Light Photocatalysts. *Langmuir* **2014**, *30*, 624−630.

(15) Jin, J.; Chen, S.; Wang, J.; Chen, C.; Peng, T. One-Pot Hydrothermal Preparation of PbO-decorated Brookite/Anatase TiO_2 Composites with Remarkably Enhanced CO_2 Photoreduction Activity. *Appl. Catal., B* **2020**, *263*, No. 118353.

(16) Sonmez, M. S.; Kumar, R. V. Leaching of Waste Battery Paste Components. Part 1: Lead Citrate Synthesis from PbO and PbO_2. *Hydrometallurgy* **2009**, *95*, 53−60.

(17) Gong, Y.; Dutrizac, J.; Chen, T. T. The Conversion of Lead Sulphate to Lead Carbonate in Sodium Carbonate Media. *Hydrometallurgy* **1992**, *28*, 399−421.

(18) Yuan, K.; Lee, S. S.; Andrade, V. D.; Sturchio, N. C.; Fenter, P. Replacement of Calcite ($CaCO_3$) by Cerussite ($PbCO_3$). *Environ. Sci. Technol.* **2016**, *50*, 12984−12991.

(19) Shirota, Y.; Niki, K.; Shindo, H. Stabilities of Crystal Faces of Aragonite-Type Strontianite ($SrCO_3$) and Cerussite ($PbCO_3$) Compared by AFM Observation of Facet Formation in Acid. *J. Crystal Growth* **2011**, *324*, 190−195.

(20) Noel, J. D.; Wang, Y.; Giammar, D. E. Effect of Water Chemistry on the Dissolution Rate of the Lead Corrosion Product Hydrocerussite. *Water Res.* **2014**, *54*, 237−246.

(21) Guo, D.; Robinson, C.; Herrera, J. E. Role of Pb(II) Defects in the Mechanism of Dissolution of Platternite (β-PbO_2) in Water under Depleting Chlorine Conditions. *Environ. Sci. Technol.* **2014**, *48*, 12525−12532.

(22) Edwards, M.; Dudi, A. Role of chlorine and chloramine in corrosion of lead-bearing plumbing materials. *J. - Am. Water Works Assoc.* **2004**, *96*, 69−81.

(23) Brown, M. J.; Raymond, J.; Homa, D.; Kennedy, C.; Sinks, T. Association Between Children's Blood Lead Levels, Lead Service Lines, and Water Disinfection, Washington, DC, 1998−2006. *Environ. Res.* **2011**, *111*, 67−74.

(24) Roy, S.; Edwards, M. A. Preventing another lead (Pb) in drinking water crisis: Lessons form the Washington D.C. and Flint MI contamination events. *Curr. Opin. Environ. Sci. Health* **2019**, *7*, 34−44.

(25) Clark, B.; Masters, S.; Edwards, M. Profile Sampling to Characterize Particulate Lead Risks in Potable Water. *Environ. Sci. Technol.* **2014**, *48*, 6836−6843.

(26) Masters, S.; Edwards, M. Increased lead in water associated with iron corrosion. *Environ. Eng. Sci.* **2015**, *32*, 361−369.

(27) Pieper, K. J.; Tang, M.; Edwards, M. A. Flint Water Crisis Caused By Interrupted Corrosion Control: Investigating "Ground Zero" Home. *Environ. Sci. Technol.* **2017**, *51*, 2007−2014.

(28) Katner, A.; Pieper, K. J.; Lambrindou, Y.; Brown, K.; Hu, C.-Y.; Mielke, H. W.; Edwards, M. A. Weaknesses in Federal Drinking Water Regulations and Public Health Policies that Impede Lead Poisoning Prevention and Environmental Justice. *Environ. Justice* **2016**, *9*, 109−117.

(29) Olson, T. M.; Wax, M.; Yonts, J.; Heidecorn, K.; Haig, S.-J.; Yeoman, D.; Hayes, Z.; Raskin, L.; Ellis, B. R. Forensic Estimates of Lead Release from Lead Service Lines during the Water Crisis in Flint, Michigan. *Environ. Sci. Technol. Lett.* **2017**, *4*, 356−361.

(30) Pieper, K. J.; Martin, R.; Tang, M.; Walters, L.; Parks, J.; Roy, S.; Devine, C.; Edwards, M. A. Evaluating Water Lead Levels During the Flint Water Crisis. *Environ. Sci. Technol.* **2018**, *52*, 8124−8132.

(31) Powell, K. J.; Brown, P. L.; Byrne, R. H.; Gajda, T.; Hefter, G.; Leuz, A.-K.; Sjoberg, S.; Wanner, H. Chemical Speciation of Environmentally Significant Metals with Inorganic Ligands. Part 3: The Pb^{2+} + OH^{1-}, Cl^{1-}, CO_3^{2-}, SO_4^{2-}, and PO_4^{3-} Systems. *Pure Appl. Chem.* **2009**, *81*, 2425−2476.

(32) Persson, K. A.; Waldwick, B.; Lazic, P.; Ceder, G. Prediction of solid-aqueous equilibria: Scheme to combine first-principles calculations of solids with experimental aqueous states. *Phys. Rev. B* **2012**, *85*, No. 235438.

(33) Pan, W.; Pan, C.; Bae, Y.; Giammar, D. Role of Manganese in Accelerating the Oxidation of Pb(II) Carbonate Solids to Pb(IV) Oxide at Drinking Water Conditions. *Environ. Sci. Technol.* **2019**, *53*, 6699−6707.

(34) Hohenberg, P.; Kohn, W. Inhomogeneous Electron Gas. *Phys. Rev.* **1964**, *136*, No. B864.

(35) Kohn, W.; Sham, L. J. Self-Consistent Equations Including Exchange and Correlation Effects. *Phys. Rev.* **1965**, *140*, No. A1133.

(36) Rong, X.; Kolpak, A. M. Ab initio Approach for Prediction of Oxide Surface Structure, Stoichiometry, and Electrocatalytic Activity in Aqueous Solution. *J. Phys. Chem. Lett.* **2015**, *6*, 1785−1789.

(37) Bennett, J.; Jones, D.; Huang, X.; Hamers, R.; Mason, S. Dissolution of Complex Metal Oxides from First-Principles and Thermodynamics: Cation Removal from the (001) Surface of $Li(Ni_{1/3}Mn_{1/3}Co_{1/3})O_2$. *Environ. Sci. Technol.* **2018**, *52*, 5792−5802.

(38) Bennett, J. W.; Jones, D. T.; Hamers, R. J.; Mason, S. E. First-Principles and Thermodynamics Study of Compositionally Tuned Complex Metal Oxides: Cation Release from the (001) Surface of Mn-Rich Lithium Nickel Manganese Cobalt Oxide. *Inorg. Chem.* **2018**, *57*, 13300−13311.

(39) Giannozzi, P.; Baroni, S.; Bonini, N.; Calandra, M.; Car, R.; Cavazzoni, C.; Ceresoli, D.; Chiarotti, G. L.; Cococcioni, M.; Dabo, I.; et al. Quantum ESPRESSO: A Modular and Open-Source Software Project for Quantum Simulations of Materials. *J. Phys.: Condens. Matter* **2009**, *21*, No. 395502.

(40) Garrity, K. F.; Bennett, J. W.; Rabe, K. M.; Vanderbilt, D. Pseudopotentials for high-throughput DFT calculations. *Comput. Mater. Sci.* **2014**, *81*, 446−452.

(41) Vanderbilt, D. Soft Self-Consistent Pseudopotentials in a Generalized Eigenvalue Formalism. *Phys. Rev. B* **1990**, *41*, 7892−7895.

(42) Monkhorst, H. J.; Pack, J. D. Special Points for Brillouin-Zone Integrations. *Phys. Rev. B* **1976**, *13*, 5188−5192.

(43) Perdew, J. P.; Burke, K.; Ernzerhof, M. Generalized Gradient Approximation Made Simple. *Phys. Rev. Lett.* **1996**, *77*, 3865−3868.

(44) Wu, Z.; Cohen, R. E. More Accurate Generalized Gradient Approximation for Solids. *Phys. Rev. B.* **2006**, *73*, No. 235116.

(45) Tran, F.; Laskowski, R.; Blaha, P.; Schwarz, K. Performance on Molecules, Surfaces, and Solids of the Wu-Cohen GGA Exchange-Correlation Energy Functional. *Phys. Rev. B* **2007**, *75*, No. 115131.

(46) Ganesh, P.; Cohen, R. E. Pressure Induced Phase Transitions in $PbTiO_3$. *J. Phys.: Condens. Matter* **2009**, *21*, No. 064225.

(47) Paul, A.; Sun, J.; Perdew, J. P.; Waghmare, U. V. Accuracy of First-Principles Interatomic Interactions and Predictions of Ferroelectric Phase Transitions in Perovskite Oxides: Energy Functional and Effective Hamiltonian. *Phys. Rev. B* **2017**, *95*, No. 054111.

(48) Rong, X.; Parolin, J.; Kolpak, A. M. A Fundamental Relationship between Reaction Mechanism and Stability in Metal Oxide Catalysts for Oxygen Evolution. *ACS Catal.* **2016**, *6*, 1153−1158.

(49) Wander, M. C. F.; Rustad, J. R.; Casey, W. H. Influence of explicit hydration waters in calculation the hydrolysis constants for geochemically relevant metals. *J. Phys. Chem. A* **2010**, *114*, 1917−1925.

(50) Sakong, S.; Naderian, M.; Mathew, K.; Hennig, R. G.; GroB, A. Density Functional Theory Study of the Electrochemical Interface Between a Pt electrode and An Aqueous Electrolyte Using an Implicit Solvent Method. *J. Chem. Phys.* **2015**, *142*, No. 234107.

(51) Sorenson, B. A.; Hong, S. S.; Herbol, H. C.; Clancy, P. How Well Do Implicit Solvation Models Represent Intermolecular Binding Energies in Organic-Inorganic Solutions. *Comput. Mater. Sci.* **2019**, *170*, No. 109138.

(52) Wagman, D. D. E.; Halow, I.; Parker, V. B.; Bailey, S. M.; Schumm, R. H. *Selected Values of Chemical Thermodynamic Properties*; National Bureau of Standards, 1971.

(53) Tamijani, A. A.; Bjorklund, J. L.; Augustine, L. J.; Catalano, J. G.; Mason, S. E. Density Functional Theory and Thermodynamics Modeling of Inner-Sphere Oxyanion Adsorption on the Hydroxylated α-Al_2O_3(001) Surface. *Langmuir* **2020**, *36*, 13166−13180.

(54) Belsky, A.; Hellenbrandt, M.; Karen, V. L.; Luksch, P. New developments in the Inorganic Crystal Structure Database (ICSD): Accessibility in Support of Materials Research and Design. *Acta Crystallogr., Sect. B: Struct. Sci.* **2002**, *58*, 364−369.

(55) Swanson, H. E.; Fuyat, R. K. *Standard X-ray Diffraction Powder Patterns*; US Department of Commerce, National Bureau of Standards, 1953; Vol. *539*, pp 1−65.

(56) Hill, R. J. Refinement of the Structure of Orthorhombic PbO (Massicot) by Rietveld Analysis of Neutron Powder Diffraction Data. *Acta Crystallogr., Sect. C: Cryst. Struct. Commun.* **1985**, *41*, 1281−1284.

(57) Bakhtatou, A.; Ersan, F. Effects of the Number of Layers on the Vibrational, Electronic and Optical Properties of α-Lead Oxide. *Phys. Chem. Chem. Phys.* **2019**, *21*, 3868−3876.

(58) Chevrier, G.; Giester, G.; Heger, G.; Jarosch, D.; Wildner, M.; Zemann, J. Neutron Single-Crystal Refinement of Cerussite, $PbCO_3$, and Comparison with other Aragonite-Type Carbonates. *Z. Kristallogr.* **1992**, *199*, 67−74.

(59) Antao, S. M.; Hassan, I. The Orthorhombic Structure of $CaCO_3$, $SrCO_3$, $PbCO_3$, and $BaCO_3$: Linear Structural Trends. *Can. Mineral.* **2009**, *47*, 1245−1255.

(60) Ye, Y.; Smyth, J. R.; Boni, P. Crystal Structure and Thermal Expansion of Aragonite-Group Carbonates by Single-Crystal X-ray Diffraction. *Am. Mineral.* **2012**, *97*, 707−712.

(61) Jain, A.; Ong, S. P.; Hautier, G.; Chen, W.; Richards, W. D.; Dacek, S.; Cholia, S.; Gunter, D.; Skinner, D.; Ceder, G.; Persson, K. A. The Materials Project: A Materials Genome Approach to Accelerating Materials Innovaton. *APL Mater.* **2013**, *1*, No. 011022.

(62) Corum, K. W.; Huang, X.; Bennett, J. W.; Mason, S. E. Systematic Density Functional Theory Study of the Structural and Electronic Properties of Constrained and Fully Relaxed (001) Surfaces of Alumina and Hematite. *Mol. Simul.* **2017**, *43*, 406−419.

(63) Huang, X.; Bennett, J. W.; Hang, M. N.; Laudadio, E. D.; Hamers, R. J.; Mason, S. E. Ab initio Atomistic Thermodynamics Study of the (001) Surface of $LiCoO_2$ in a Water Environment and Implications for Reactivity under Ambient Conditions. *J. Phys. Chem. C* **2017**, *121*, 5069−5080.

(64) Corum, K. W.; Abbaspour-Tamijani, A.; Mason, S. E. Density Functional Theory Study of Arsenate Adsorption onto Alumina Surfaces. *Minerals* **2018**, *8*, No. 91.

(65) Li, G.; Bae, Y.; Mishra, A.; Shi, B.; Giammar, D. E. Effect of Aluminum on Lead Release to Drinking Water from Scales. *Environ. Sci. Technol.* **2020**, *54*, 6142−6151.

(66) Tully, J.; DeSantis, M. K.; Schock, M. R. Water Quality-Pipe Deposit Relationships in Midwestern Lead Pipes. *AWWA Water Sci.* **2019**, *1*, No. e1127.

(67) Lytle, D. A.; Schock, M. R. Formation of Pb(IV) Oxides in Chlorinated Water. *J. - Am. Water Works Assoc.* **2005**, *97*, 102−114.

(68) Cartier, C.; Nour, S.; Richer, B.; Deshommes, E.; Prevost, M. Impact of Water Treatment on the Contribution of Faucets to Dissolved and Particulate Lead Release at the Tap. *Water Res.* **2012**, *46*, 5205−5216.

(69) Bian, S.-W.; Mudunkotuwa, I. A.; Rupasinghe, T.; Grassian, V. H. Aggregation and Dissolution of 4nm ZnO Nanoparticles in Aqueous Environments: Influence of pH, Ionic Strength, Size, and Adsorption of Humic Acid. *Langmuir* **2011**, *27*, 6059−6068.

(70) Lowry, G. V.; Gregory, K. B.; Apte, S. C.; Lead, J. R. Transformations of Nanomaterials in the Environment. *Environ. Sci. Technol.* **2012**, *46*, 6893−6899.

(71) Levard, C.; Hotze, E. M.; Lowry, G. V.; G. E. Brown, J. Environmental Transformations of Silver Nanoparticles: Impact on Stability and Toxicity. *Environ. Sci. Technol.* **2012**, *46*, 6900−6914.

(72) Grassian, V. H.; et al. NanoEHS—defining fundamental science needs: no easy feat when the simple itself is complex. *Environ. Sci.: Nano* **2016**, *3*, 15−27.

(73) Mudunkotuwa, I. A.; Grassian, V. H. Biological and environmental media control oxide nanoparticle surface composition: the roles of biological components (proteins and amino acids), inorganic oxyanions and humic acid. *Environ. Sci.: Nano* **2015**, *2*, 429−439.

(74) Buchman, J. T.; Bennett, E. A.; Wang, C.; Abbaspour-Tamijani, A.; Bennett, J. W.; Hudson, B.; Green, C.; Clement, P.; Zhi, B.; Henke, A.; Laudadio, E.; Mason, S. E.; Hamers, R.; Klaper, R.; Haynes, C. Nickel Enrichment of Next-Generation NMC Nanomaterials Alters Material Stability, Causing Unexpected Dissolution Behavior and Observed Toxicity to S. Oneidensis MR-1 and D. Magna. *Environ. Sci.: Nano* **2020**, *7*, 571−587.

(75) Bennett, J. W.; Jones, D. T.; Hudson, B. G.; Melendez-Rivera, J.; Hamers, R. J.; Mason, S. E. First-Principles and Thermodynamics Comparison of Compositionally-Tuned Delafossites: Cation Release from the (001) Surface of Complex Metal Oxides. *Environ. Sci.: Nano* **2020**, *7*, 1642−1651.

(76) Abbaspour-Tamijani, A.; Bennett, J. W.; Jones, D. T.; Cartagena-Gonzalez, N.; Jones, Z. R.; Laudadio, E. D.; Hamers, R. J.; Santana, J. A.; Mason, S. E. DFT and Thermodynamics Calculations of Surface Cation Release in $LiCoO_2$. *Appl. Surf. Sci.* **2020**, *515*, No. 145865.

(77) Hopwood, J. D.; Derrick, G. R.; Brown, D. R.; Newman, C. D.; Haley, J.; Kershaw, R.; Collinge, M. The Identification and Synthesis of Lead Apatite Minerals Formed in Lead Water Pipes. *J. Chem.* **2016**, *2016*, No. 9074062.

(78) Bae, Y.; Pasteris, J. D.; Giammar, D. E. Impact of Orthophosphate on Lead Release from Pipe Scale in High pH, Low Alkalinity Water. *Water Res.* **2020**, *177*, No. 115764.

(79) Arnold, R. B.; Edwards, M. Potential Reversal and the Effects of Flow Pattern on Galvanic Corrosion of Lead. *Environ. Sci. Technol.* **2012**, *46*, 10941−10947.

(80) Stets, E. G.; Lee, C. J.; Lytle, D. A. Increasing chloride in rivers of the conterminous U.S. and linkages to potential corrosivity and lead action level exceedances in drinking water. *Sci. Total Environ.* **2018**, *613−614*, 1498−1509.

(81) Pieper, K. J.; Tang, M.; Jones, C. N.; Weiss, S.; Greene, A.; Mohsin, H.; Parks, J.; Edwards, M. A. Impact of Road Salt on Drinking Water Quality and Infrastructure Corrosion in Private Wells. *Environ. Sci. Technol.* **2018**, *52*, 14078−14087.

(82) Mason, S. E.; Iceman, C. R.; Tanwar, K. S.; Trainor, T. P.; Chaka, A. M. Pb(II) adsorption on isostructural hydrated alumina and hematite (0001) surfaces: A DFT study. *J. Phys. Chem. C* **2009**, *113*, 2159−2170.

(83) Mason, S. E. Fundamental Insights About Environmental Interface Reactivity from DFT Calculations of Geochemical Model Systems. *Surf. Sci.* **2015**, *631*, 48−56.

(84) Du, H.; Qu, C.; Ma, M.; Lei, M.; Tie, B.; Liu, X.; Wei, X.; Yang, Y. Insights into Pb(II) Binding by Fe/Al Hydroxide-Microbe Composite: XAFS Spectroscopy and Isothermal Titration Calorimetry Study. *Chem. Geol.* **2019**, *510*, 84−90.

(85) Wu, J.; Zhao, X.; Li, Z.; Gu, X. Thermodynamic and Kinetic Coupling Model of Cd(II) and Pb(II) Adsorption and Desorption on Goethite. *Sci. Total Environ.* **2020**, *727*, No. 138730.

(86) Towns, J.; Cockerill, T.; Dahan, M.; Foster, I.; Gaither, K.; Grimshaw, A.; Hazlewood, V.; Lanthrop, S.; Lifka, D.; Peterson, G. D.; Roskies, R.; Scott, J. R.; Wilkins-Diehr, N. XSEDE:Accelerating Scientific Discovery. *Comput. Sci. Eng.* **2014**, *16*, 62−74.